Supplementary Information (SI) for ChemComm.

Ni-Fe-Mo Oxide Bifunctional Electrocatalysts Enabling High Efficiency Overall Water Splitting in Alkaline Media

Notes

1. Experimental details

Materials and chemicals

All chemicals used were of analytical grade and utilized without further purification. NF was purchased from Kunshan Guang Jia Yuan New Material Co., Ltd. Sinopharm Group Chemical Reagent Co. supplied ferrous sulfate heptahydrate ($FeSO_4 \cdot 7H_2O$), nickel(II) nitrate hexahydrate ($Ni(NO_3)_2 \cdot 6H_2O$), ammonium molybdate tetrahydrate ($(NH_4)_6Mo_7O_{24} \cdot 4H_2O$), and sodium dodecyl benzene sulfonate ($C_{18}H_{29}NaO_3S$) was purchased from Tianjin Bodi Chemical Co., Ltd. Seawater samples were collected from the Bohai Sea.

Preparation of Ni-Fe-Mo oxide precursors

To prepare the Ni-Fe-Mo oxide precursor, 0.75 mmol $FeSO_4 \cdot 7H_2O$, 0.75 mmol $Ni(NO_3)_2 \cdot 6H_2O$, 0.75 mmol $(NH_4)_6Mo_7O_{24} \cdot 4H_2O$, and 0.25 g $C_{18}H_{29}NaO_3S$ were dissolved in 30 mL of deionized water in a 50 mL Teflon-lined autoclave. The solution was stirred for 30 min, after which a piece of NF was immersed in the solution. The autoclave was sealed and heated at 120 °C for 48 h. Upon cooling to room temperature, the sample was washed thoroughly with ethanol and deionized water and then dried under vacuum at 60 °C for 12 h. The resulting material $(NiFe)_2O_3/(NiFe)_2(MoO_4)_3$ was designated as Ni-Fe-Mo precursor, abbreviated as Ni-Fe-Mo pre.

Preparation of Ni-Fe-Mo oxides

The Ni-Fe-Mo precursor was placed in a porcelain boat and positioned at the center of a tube furnace. The sample was purged with an H_2/Ar atmosphere (5% H_2 and 95% Ar) for 15 min, heated to 450 °C at a ramping rate of 5 °C min^{-1}, and maintained at this temperature for 2 h. After natural cooling to room temperature, Ni-Fe-Mo oxide hybrids were obtained and designated as Ni-Fe-Mo O. For comparison, Ni-Fe O and Fe-Mo O were prepared following the same process.

Characterization

The surface morphology of the samples was observed using a JEOL JSM-6700F scanning electron microscope (SEM). The internal structure, crystal structure, morphology, and defects of the samples were characterized using a JSM-JEM-2100F transmission electron microscope (TEM). X-ray diffraction (XRD) analysis was conducted using a D-MAX2500/PC diffractometer with Cu-Kα radiation ($\lambda = 0.15418$ nm) to determine the crystal structure of the samples. X-ray photoelectron spectroscopy (XPS) was performed on a Thermo ESCALAB 250Xi spectrometer with Al Kα radiation (1846.6 eV) to evaluate the valency states and surface elemental composition. All catalyst-loaded samples were ultrasonically exfoliated in ethanol, followed by centrifugation to isolate powdered materials for subsequent characterization.

2． Electrochemical characterizations

Electrochemical measurements were conducted using a conventional three-electrode setup on a CHI 760E electrochemical workstation (Shanghai Chenhua, China). A Hg/HgO electrode served as the reference electrode, a carbon rod as the counter electrode, and the NF-loaded sample as the working electrode. The alkaline seawater electrolyte contained 1.0 M KOH and natural seawater (1.0 M KOH + seawater).

Before measurements, N_2 was bubbled through the electrolyte for 30 min. Linear sweep voltammetry (LSV), Tafel analysis, electrochemical impedance spectroscopy (EIS), and stability tests were performed. LSV measurements were conducted at a sweep rate of 5 mV s^{-1}, with IR compensation applied using the equation: $E_{IR\text{-}corrected} = E_{RHE} - IR$. All measured potentials were converted to the Reversible Hydrogen Electrode (RHE) potential using the equation: $E_{(RHE)} = E_{(Hg/HgO)} + 0.0591 \times pH + 0.118$. The overpotential ($\eta$) for the OER was calculated as: $\eta = E_{RHE} - 1.23$.

To determine double-layer capacitance (C_{dl}) with electrochemical surface area (ECSA), cyclic voltammetry (CV) was conducted at sweep rates of 5, 10, 15, 20, and 25 $mV \cdot s^{-1}$ in the non-Faraday region. EIS measurements were performed across a frequency range of 10^{-2} to 10^5 Hz to assess charge transfer resistance. Durability was evaluated using chronopotentiometry.

For overall water-splitting performance, a two-electrode setup was constructed with the catalyst serving as both the cathode and anode. Commercial Pt/C and RuO_2 were used as reference electrodes for comparison.

Figures

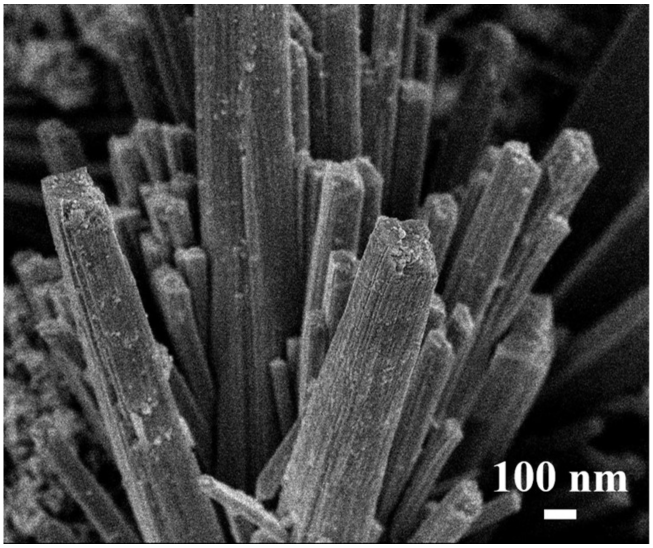

Fig. S1 SEM image of Ni-Fe-Mo pre.

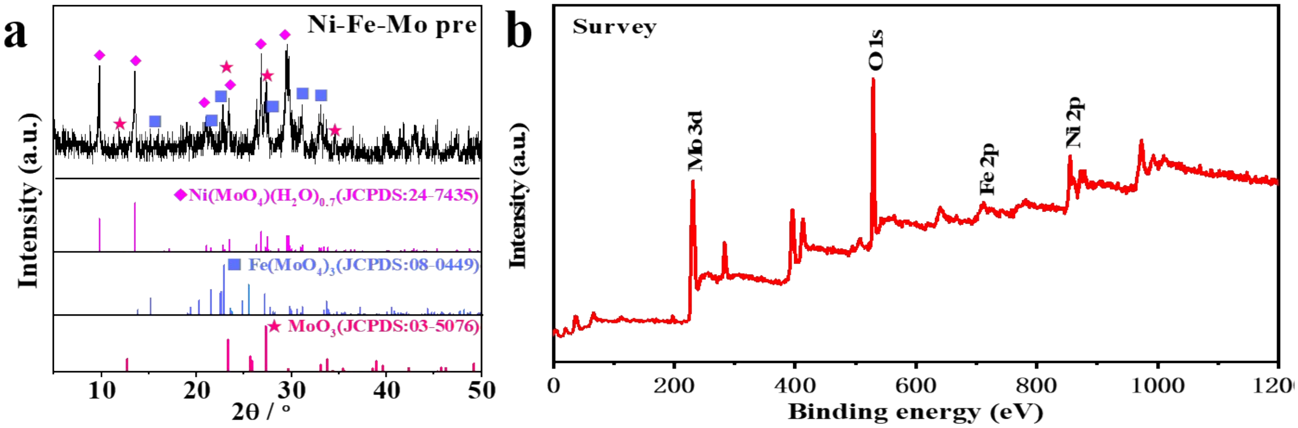

Fig. S2 (a) XRD patterns of Ni-Fe-Mo pre; (b) XPS survey spectrum of Ni-Fe-Mo O.

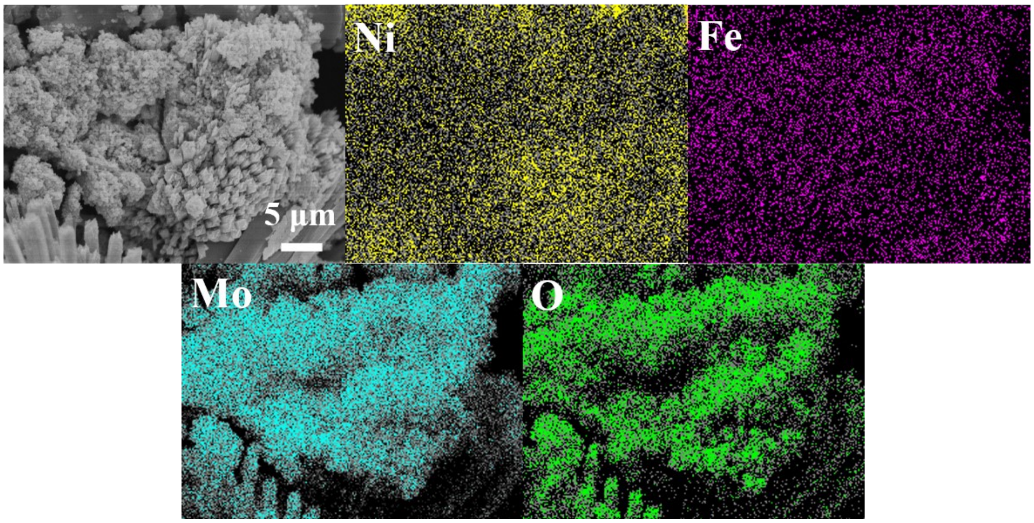

Fig. S3 SEM image of Ni-Fe-Mo O and corresponding EDS elemental mapping images.

Elemental distribution analysis via EDS (Fig. S3) reveals that the four elements-Ni, Fe, Mo, and O-are uniformly distributed across Ni-Fe-Mo O. This uniform distribution enhances the active surface area of the catalyst, improving the efficiency of catalytic reactions. Mo and O dominate the composition of the nanorods, while Ni and Fe are less abundant and more scattered across the nanorod surface. These results suggest that MoO_2 and $(FeO)_2(MoO_2)_3$ are integrated to form the nanorod structure.

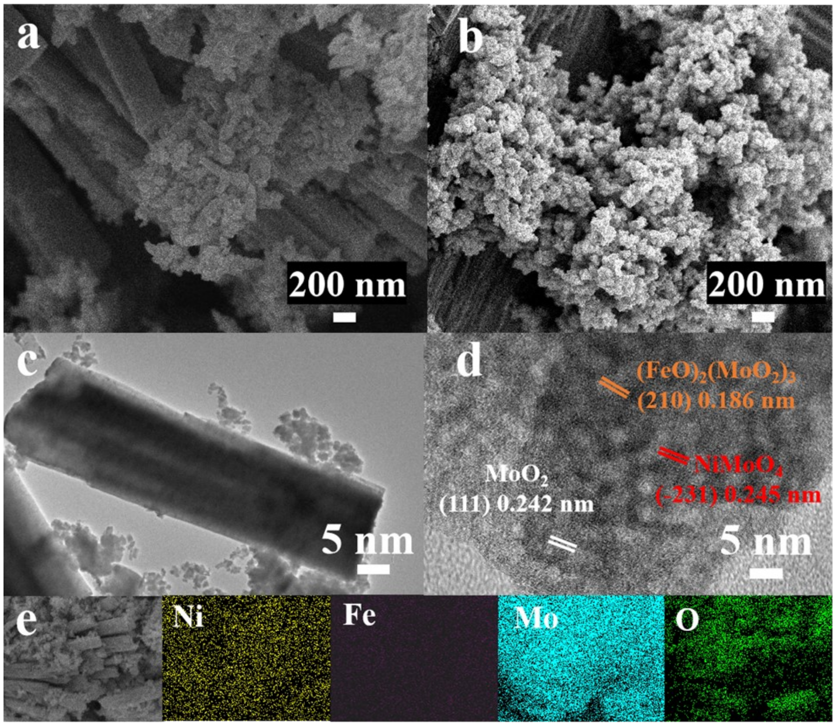

Fig. S4 (a, b) SEM images of post-test Ni-Fe-Mo O; (c, d) TEM images of post-test Ni-Fe-Mo O; (e) SEM image of Ni-Fe-Mo O with corresponding EDS elemental mapping.

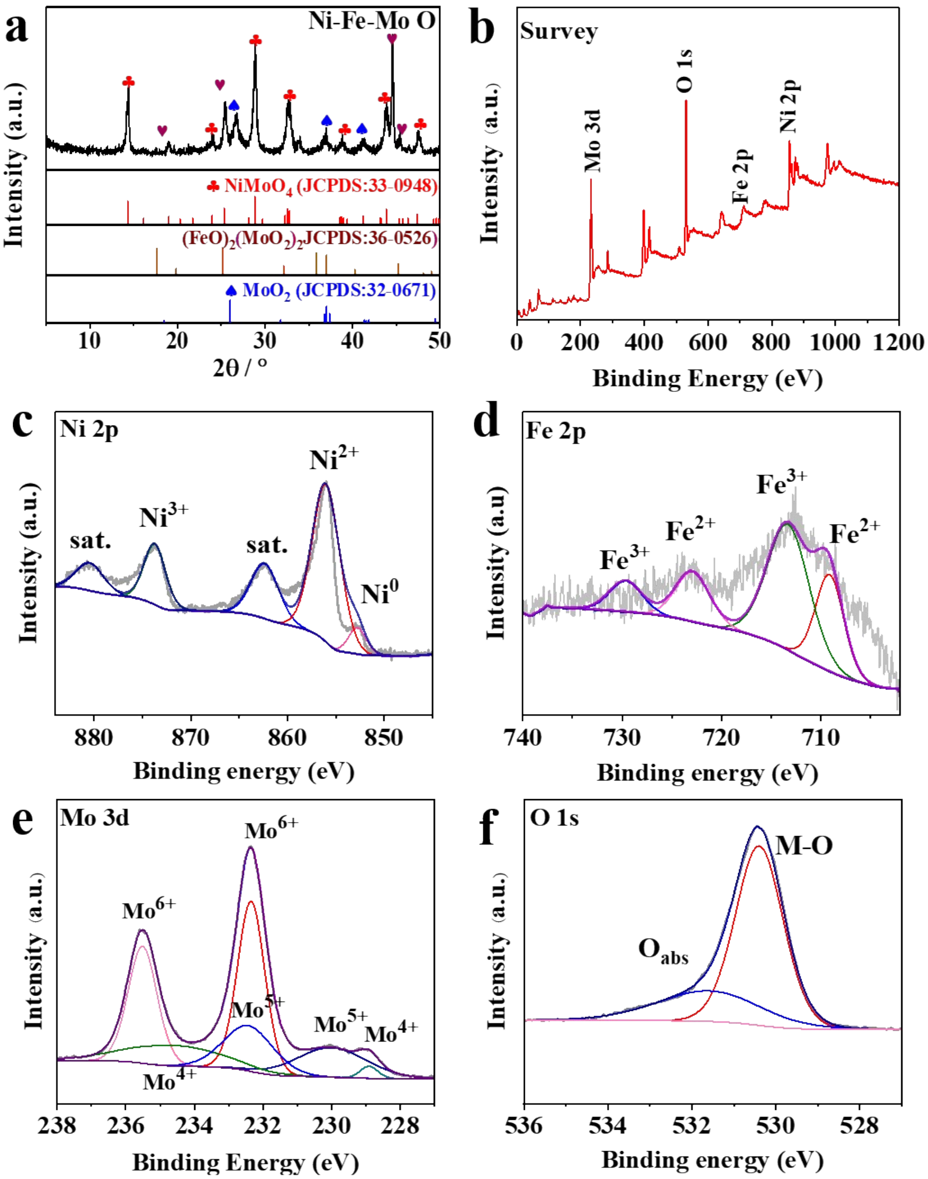

Fig. S5 (a) XRD pattern of post-test Ni-Fe-Mo O; (b) XPS survey spectrum of post-test Ni-Fe-Mo O; high-resolution XPS spectra with peak fitting for (c) Ni 2p, (d) Fe 2p, (e) Mo 3d, and (f) O 1s.

As shown in Fig. S4, post-electrolysis TEM, SEM, and EDX analyses confirm that the Ni-Fe-Mo O catalyst maintains its original morphology and phase composition after 35 h of HER/OER operation. SEM images (Fig. S4a-b) reveal no structural collapse or agglomeration of nanorods and nanoparticles, while TEM (Fig. S4c-d) shows unchanged lattice spacings (e.g., 0.242 nm for MoO_2, 0.246 nm for $NiMoO_4$, 0.186 nm for $(FeO)_2(MoO_2)_3$), consistent with pre-electrolysis data. EDX mapping (Fig. S4e) confirms uniform elemental distribution (Ni, Fe, Mo, O) without signs of dissolution or segregation. These findings align with the XRD phase stability discussed earlier, collectively demonstrating robust structural and compositional integrity during prolonged electrolysis.

Post-electrolysis XRD patterns (Fig. S5a) further confirm structural integrity, showing no new peaks or phase transformations after extended testing. The diffraction peaks remain consistent with $NiMoO_4$ (JCPDS: 33-0948), $(FeO)_2(MoO_2)_2$ (JCPDS: 36-0526), and MoO_2 (JCPDS: 32-0671), evidencing excellent phase stability under operational conditions.

High-resolution XPS spectra (Fig. S5c-f) show negligible changes in the chemical states of Ni^{2+} (Ni $2p_{3/2}$ at 855.8 eV), Fe^{3+} (Fe $2p_{3/2}$ at 711.5 eV), and Mo^{6+} (Mo $3d_{5/2}$ at 232.6 eV). The absence of Cl 2p signals (198-200 eV) rules out chloride adsorption or corrosion product formation.

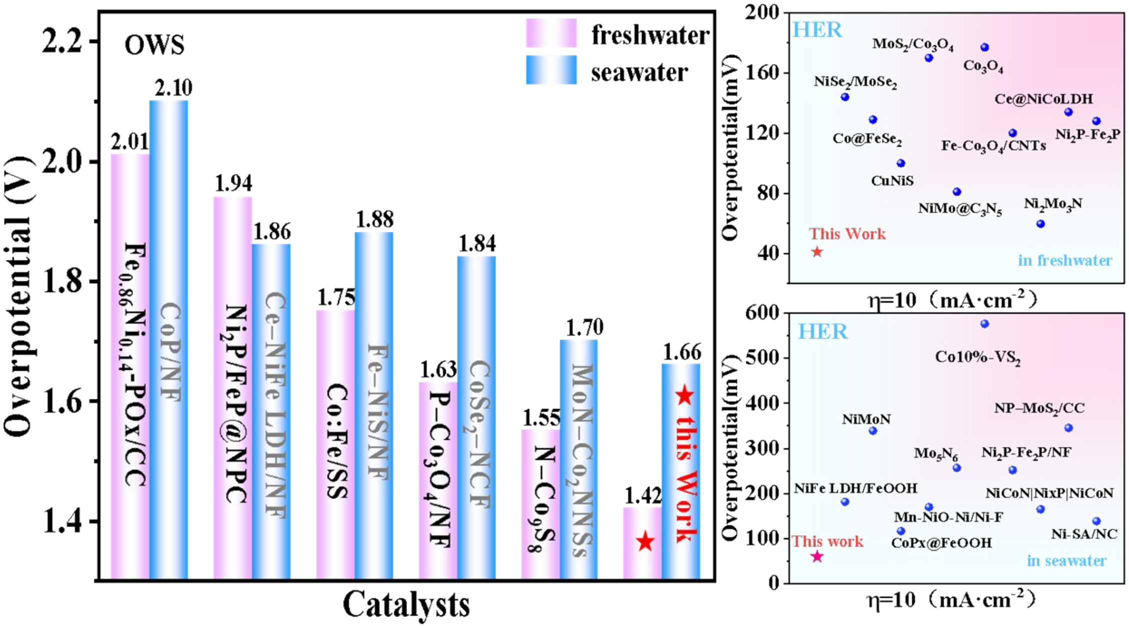

Fig. S6 Comparison of overall water splitting and HER performance at 10 mA·cm^{-2} for Ni-Fe-Mo O in freshwater and seawater electrolytes.

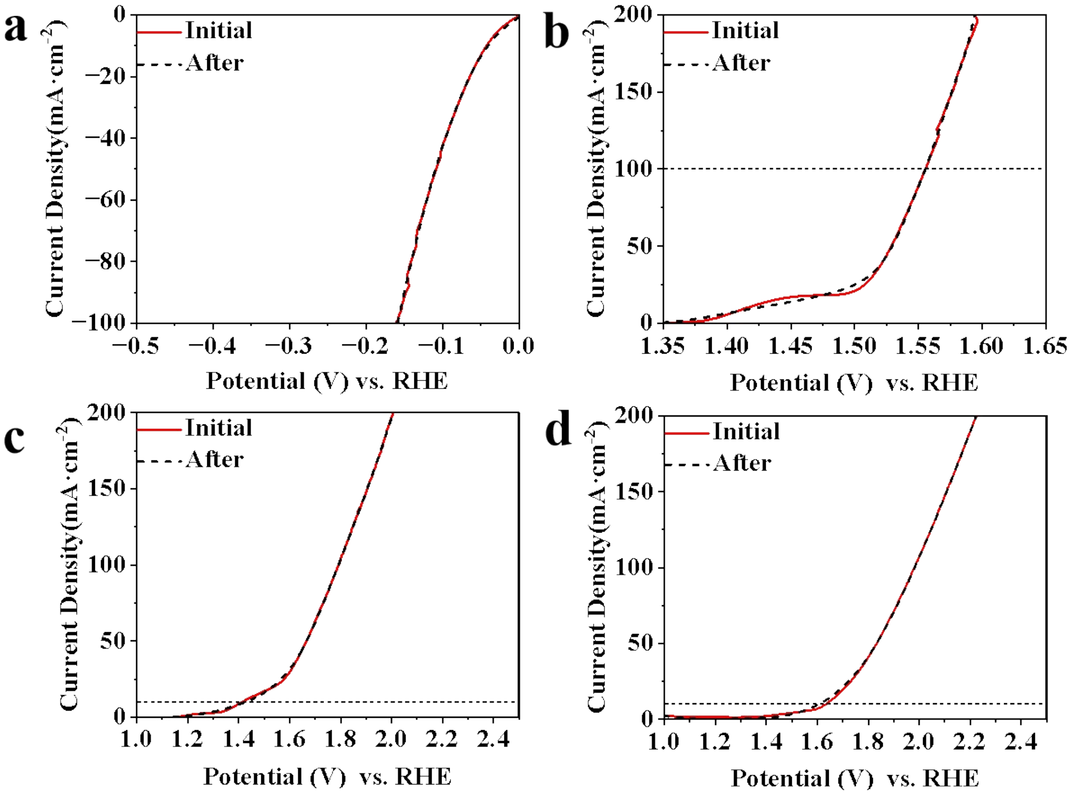

Fig. S7 LSV plots of Ni-Fe-Mo O before and after electrolysis: (a) after 35-hour HER; (b) after 35-hour OER. LSV plots before and after 35-hour chronoamperometric stability tests at 10 mA·cm^{-2} in: (c) 1.0 M KOH; (d) 1.0 M KOH + seawater electrolyte.

The LSV curves recorded after the 35-hour HER test (at -10 mA·cm^{-2}) show negligible overpotential shifts ($\Delta\eta < 10$ mV), indicating excellent retention of HER activity. Similarly, post-OER testing reveals minimal overpotential increase ($\Delta\eta \approx 15$ mV) at +10 mA·cm^{-2}, confirming the catalyst's robust structural and electrochemical stability under prolonged oxidative conditions.

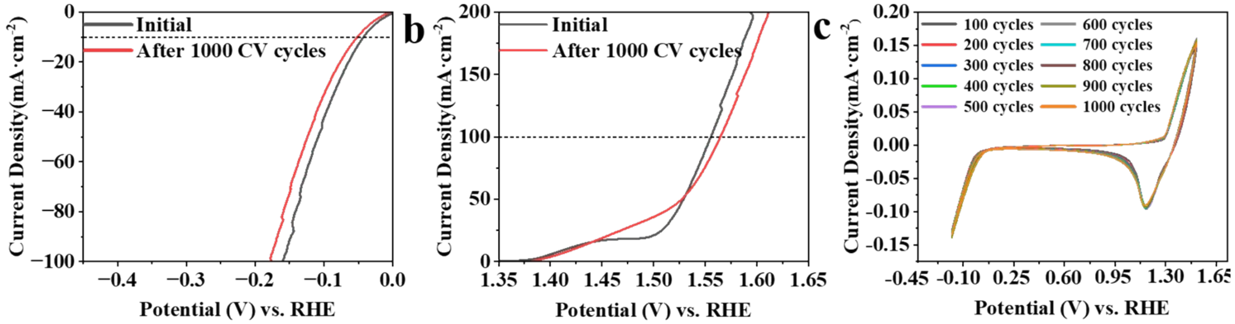

Fig. S8 LSV curves of Ni-Fe-Mo O film before and after 1000 CV cycles in 1.0 M KOH for: (a) HER and (b) OER. (c) Representative CV curves at selected cycles (100 - 1000), recorded at a sweep rate of 50 mV.s^{-1}.

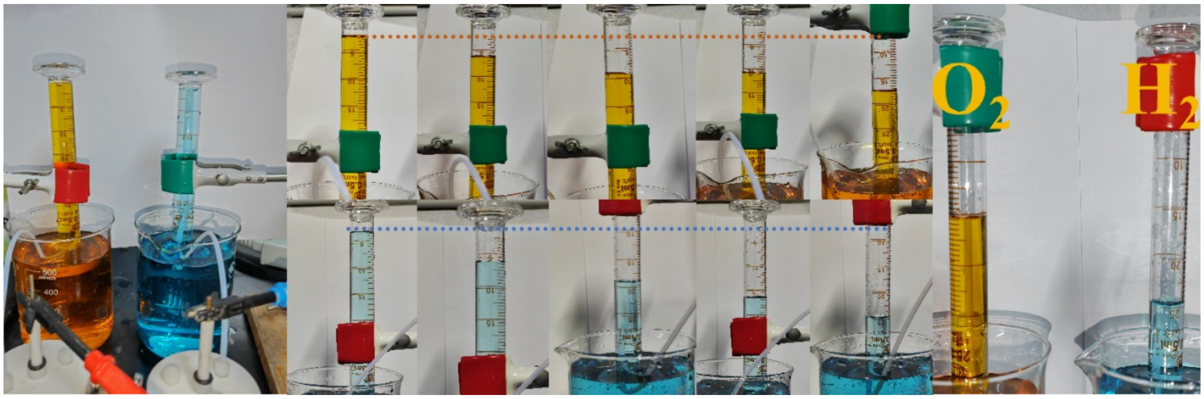

Fig. S9 Schematic of the Faradaic efficiency measurement setup for water splitting, along with photographs showing the collected H_2 and O_2 gases.

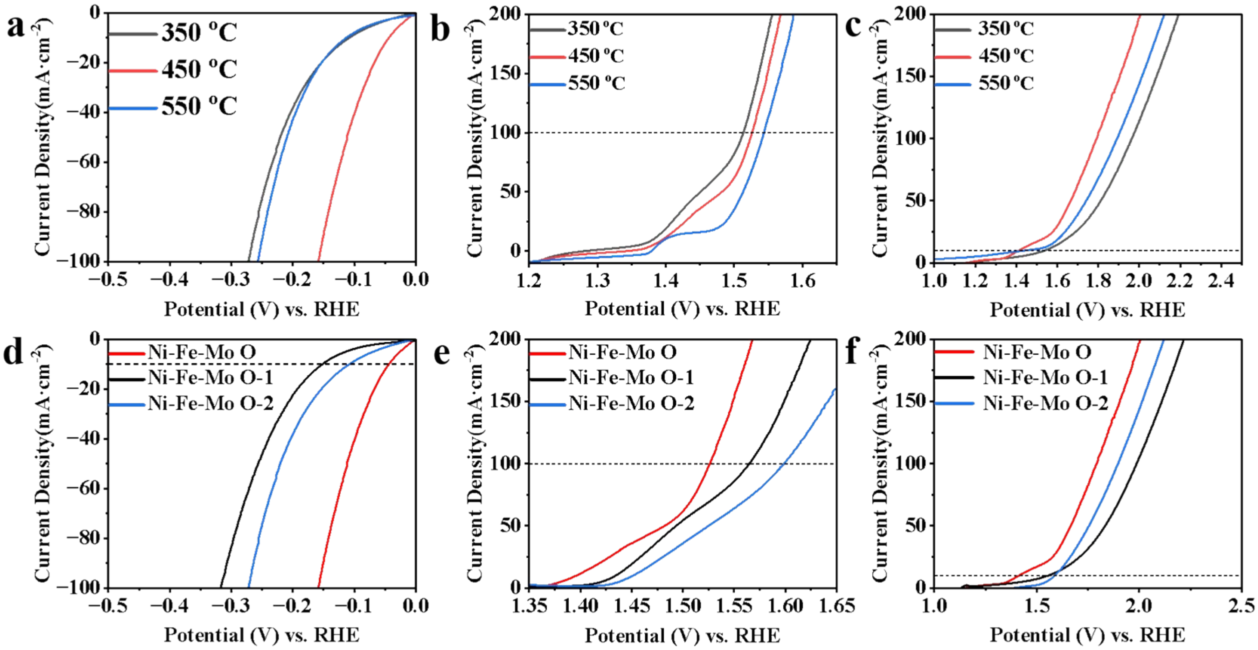

Fig. S10 (a-c) LSV curves for HER, OER, and OWS of Ni-Fe-Mo O under temperature gradients; (d-f) LSV curves for HER, OER, and OWS under concentration gradients.

The effects of temperature and concentration gradients were systematically investigated. Calcination temperature was first optimized by comparing samples treated at 350 °C, 450 °C, and 550 °C. The catalyst calcined at 450 °C exhibited the best catalytic performance for both HER and OER. Additionally, stoichiometric variation tests (±15% deviation from the nominal Ni: Fe: Mo =1: 1: 7 ratio) revealed that the original composition delivered the highest bifunctional activity, while modified ratios (Ni-Fe-Mo O-1: 0.85: 0.85: 5.95; Ni-Fe-Mo O-2: 1.15: 1.15: 8.05) showed diminished HER/OER kinetics. All syntheses were conducted under tightly controlled conditions to ensure reproducibility.

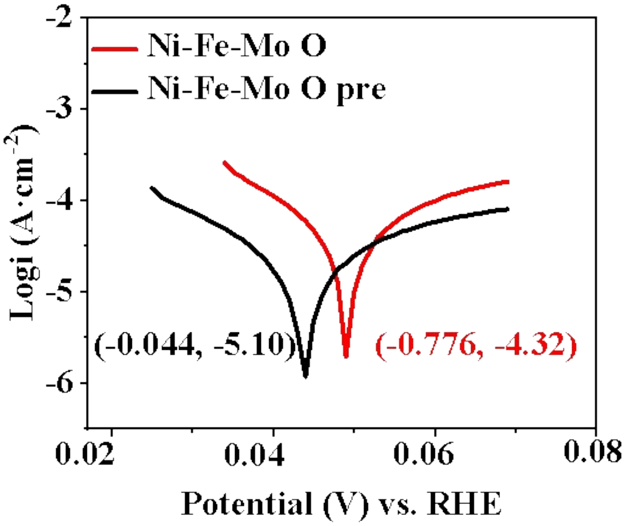

Fig. S11 Tafel polarization curves for corrosion current measurements of Ni-Fe-Mo O and Ni-Fe-Mo pre in 1.0 M KOH + seawater.

Tafel measurements were conducted (Fig. S11) for Ni-Fe-Mo pre and Ni-Fe-Mo O in 1.0 M KOH + seawater. Ni-Fe-Mo O exhibited a higher self-corrosion potential and lower corrosion current density, indicating enhanced chloride corrosion resistance, attributable to suppressed corrosion kinetics and improved thermodynamic stability.

Table S1 Comparison of HER and OER activities of the present work with other catalysts in 1.0 M KOH.

HER electrocatalysts	η (mV)	Ref	**OER** electrocatalysts	η (mV)	Ref
Ni-Fe-Mo O	**η_{10}= -41**	**This work**	**Ni-Fe-Mo O**	**η_{100}=320**	**This work**
Ni/MoN@NCNT/CC	η_{10}= -207	1	MoP@Ni_3P/NF	η_{10}=331	11
PdO@Co_2FeO_4	η_{10}= -269	2	$CuCo_2O_4$/NrGO	η_{10}=360	12
Co_2P	η_{10}= -280	3	Ti_3C_2-CoS_2	η_{100}=376	13
MoS_2 /Co_3O_4	η_{10}= -170	4	Mo-CoP	η_{100}=330	14
Co,V-FeNi-LDH	η_{10}= -180	5	Co-NC@Mo_2C	η_{10}=347	15
NiFeLDH@NiCoP	η_{10}= -120	6	$NiCo_2O_4$/NiCoP	η_{10}=369	16
MoNiNC	η_{10}= -110	7	CeO_2@NiCo-OH/NF	η_{100}=431	17
MoS_2/NiS/MoO_3	η_{10}= -91	8	$CoTe_2$/TM	η_{100}=340	18
$CoMoO_4$ NW	η_{10}= -81	9	CoP NPs/C	η_{10}=330	19
Ni/Mo LDH@P-rGO	η_{10}= -91	10	S-Co NPs/CNS	η_{10}=320	20

[1] P. Wang, J. Qi, C. Li, X. Chen, T. Wang and C. Liang, ChemElectroChem, 2020, 7, 745-752.

[2] M . Y. Solangi, U. Aftab, A. Tahira, M. I. Abro, R. Mazarro, V.Morandi, A. Nafady, S. S. Medany, A. Infantes-Molina and Z. H. Ibupoto, Int. J. Hydrogen Energy, 2022, 47, 3834-3845.

[3] H. Li, Q. Li, P. Wen, T. B. Williams, S. Adhikari, C. Dun, C. Lu, D. Itanze, L. Jiang, D. L. Carroll, G. L. Donati, P. M. Lundin,Y. Qiu and S. M. Geyer, J. Adv. Mater., 2018, 30,1705796.

[4] X. Sun , J. Huo , Y. Yang , L. Xu , S. Wang, J. Energy Chem, 2017, 26(6): 1136-1139.

[5] F. Zheng, M A. Gaikwad, Z. Fang, S. Jang, JH. Kim, Energy & Fuels, 2024, 38(7): 6290-6299.

[6] H. Zhang, X. Li, A. Hähnel, V. Naumann, C. Lin, S. Azimi, S.L. Schweizer, A.W. Maijenburg, R.B. Wehrspoh, Adv. Funct. Mater 28, (14) (2018) 1706847.

[7] F. Wang, Y. Sun, Y. He, L. Liu, J. Xu, X. Zhao, G. Yin, L. Zhang, S. Li, Q. Mao,Y. Huang, T. Zhang, B. Liu, Nano Energy, 2017,37: 1-6.

[8] C. Wang, B. Tian, M. Wu, J. Wang, ACS Appl. Mater. Interfaces, 2017, 9(8): 7084-7090.

[9] J. Zhao, X. Ren, H. Ma, X. Sun, Y. Zhang, T. Yan, Q. Wei, D. Wu, ACS Sustain. Chem. Eng, 2017, 5(11): 10093-10098.

[10] P. Salehan, S. Niknazar, A A. Ensafi, K Z. Mousaabadi, B. RezaeiInt. J. Hydrogen Energy, 2023, 48(67): 26200-26209.

[11] F. Wang, J. Chen, X. Qi, H. Yang, H. Jiang, Y. Deng and T. Liang, Appl. Surf. Sci., 2019, 481, 1403-1411.

[12] S. K. Bikkarolla and P. Papakonstantinou, J. Power Sources, 2015, 281, 243-251.

[13] S. B. Devi and R. Navamathavan, J. Electrochem. Soc., 2023, 170(9): 096503.

[14] S. M. Li, L. Bai, H. B. Shi, X. F. Hao, L. Chen, X. J. Qin and G. J. Shao, Ionics, 2021, 27, 3109-3118.

[15] Q. Liang, H. Jin, Z. Wang, Y. Xiong, S. Yuan, X. Zeng, D. He and S. Mu, Nano Energy, 2019, 57, 746-752.

[16] W. Jin, J. Chen, H. Wu, N. Zang, Q. Li, W. Cai and Z. Wu, Catal. Sci. Technol., 2020, 10(16): 5559-5565.

[17] H. Sun, B. Jin, S. Cao, J. Zhang, T. Li, X. Liu, G. Liu, J. Li, J. Electroanal. Chem., 2023, 943: 117591.

[18] N-T. Suen, S-F. Hung, Q. Quan, N. Zhang, Y-J. Xu, HM, Chen. Chem Soc Rev., 2017;46(2):337-65.

[19] Y. Bai, H. Zhang, Y. Feng, L. Fang and Y. Wang. J. Mater. Chem. A, 2016, 4(23): 9072-9079.

[20] M. Al-Mamun, Z. Zhu, H. Yin, X. Su, H. Zhang, P. Liu,.H. Yang, D. Wang, Z. Tang, Y. Wang and H. Zhao. Chem. Commun., 2016, 52(60): 9450-9453.

Acknowledgements

This work was supported by the National Natural Science Foundation of China (21905153, 22378221, 22308183, 52002198, 21776147, 61604086), the Natural Science Foundation of Shandong Province (ZR2021YQ32, ZR2023QB070), the Taishan Scholar Project of Shandong Province (tsqn201909117), the Qingdao Science and Technology Benefit the People Demonstration and Guidance Special Project (23-2-8-cspz-11-nsh), the Qingdao Natural Science Foundation (23-2-1-241-zyyd-jch), the China Postdoctoral Science Foundation (2023M731856), and the research fund of the Key Laboratory of Fuel Cell Technology of Guangdong Province. L. F. Dong also thanks financial support from the Malmstrom Endowed Fund at Hamline University.